Journal of Solid State Electrochemistry (2024) 28:4077–4086
https://doi.org/10.1007/s10008-024-05946-y

ORIGINAL PAPER

Reduced graphene oxide film modified by tannic acid for high areal performance supercapacitors

Wei Wang[1,2] · Qiang Li[1] · Yage Pan[1] · Chuanren R. Ye[3] · Xingnian Li[1] · Yingyu Chen[1] · Qiong Tang[1] · Jun Xu[2] · Yanwu Zhu[3]

Received: 10 April 2024 / Revised: 19 May 2024 / Accepted: 22 May 2024 / Published online: 16 July 2024

Abstract

When graphene oxide (GO) was reduced, the stacking of reduced graphene oxide (rGO) sheets would lead to far lower of its specific capacitance than the theoretical value of graphene. In order to solve this problem, we use tannic acid (TA) to modify the rGO layered film by vacuum filtration of the mixture of GO and TA in solution, and then mild thermal reduction at 180℃. Due to the rich redox active functional groups of TA, the introduction of TA can not only alleviate the stacking of rGO sheets and promote the reduction process of GO at relatively low temperature, but also provide additional pseudocapacitance. When used for two-electrode symmetrical supercapacitor in 6 M KOH electrolyte, the TrGO-0.5 gives areal capacitance of 525 mF cm^{-2}, and energy density of 72.2 uWh cm^{-2} at power density of 250.9 uW cm^{-2}. It also has capacitance retention of 91.7% after 10,000 charging/discharging cycles at current density of 4 mA cm^{-2}. The TrGO-0.5 based button cell with 2 M 1-ethyl-3-methylimidazole tetrafluoroborate ($EMIMBF_4$) as electrolyte shows the practical application to light up three LEDs.

Keywords Reduced graphene oxide · Tannic acid · Areal capacitance · Cycling stability · Supercapacitor

Introduction

Electrochemical energy storage devices become more and more important in modern society, many devices, such as new energy electric vehicles and portable wireless network products, depend on them for energy support [1–3]. Supercapacitors are electrochemical energy storage devices, compared to batteries, supercapacitors have higher power density, shorter charging time, and longer cycle life, but lower energy density [4–6]. Based on the electrode materials and their energy storage mechanisms, supercapacitors can be divided into electric double layer (EDL) capacitors and pseudocapacitors [7, 8]. Over the past few decades, researchers have focused on designing and fabricating different kinds of electrode materials for supercapacitors. Carbon materials, such as activated carbon [9, 10], carbon nanotubes [11, 12] and graphene [13, 14], are usually used as electrodes in EDL capacitors, and they store energy by accumulating charges at the interfaces of electrode and electrolyte. Conducting polymers (polyaniline [15, 16], polypyrrole [17, 18], polyacetylene [19, 20], etc.) and transition metal oxides (MnO_2 [21], RuO_2 [22], Fe_2O_3 [23], etc.) are the typical electrode materials for pseudocapacitors, with Faradaic reaction as the underlying mechanism [24]. Therefore, EDL capacitors generally exhibit better rate capability and cycling stability, but pseudocapacitors have relatively higher specific capacitance. Due to its excellent conductivity and high theoretical surface area (2630 $m^2 g^{-1}$), graphene is the ideal electrode material for EDL capacitros [25, 26]. However, the π-π interaction between graphene sheets leads to the stacking of rGO sheets during the reduction process from GO to rGO [27], resulting in the inability to fully utilize their surface area. Introducing intercalator materials between graphene sheets, such as transition metal oxides [28, 29], conducting polymers

✉ Qiang Li
qli@hfut.edu.cn

✉ Chuanren R. Ye
ycr19@ustc.edu.cn

[1] School of Physics, Hefei University of Technology, Hefei 230009, Anhui, China

[2] School of Microelectronics, Hefei University of Technology, Hefei 230009, Anhui, China

[3] Hefei National Research Center for Physical Sciences at the Microscale & CAS Key Laboratory of Materials for Energy Conversion, Department of Materials Science and Engineering, University of Science and Technology of China, Hefei 230026, Anhui, China

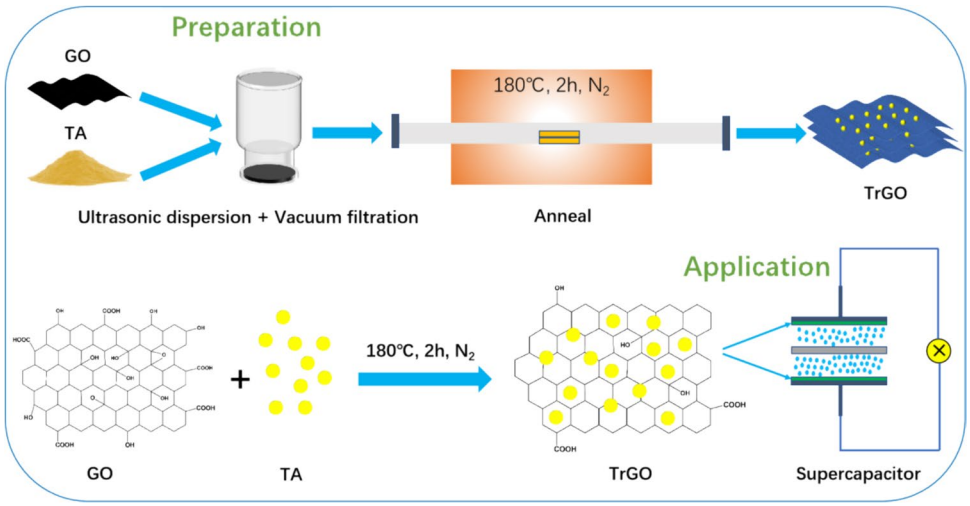

Fig. 1 Schematic illustration of fabricating the TrGO film and its application for supercapacitor

[30, 31], and other carbon materials [32–34], as functional components can prevent the stacking of graphene sheets. The synergistic effect between graphene and the intercalator materials makes the graphene-based composites to give better electrochemical performance.

Tannic acid (TA) is an organic molecule which can exhibit redox activity. It mainly consists of derivatives of gallic acid, and sources from various plants such as oak. Because TA is safe, non-toxic, and cost-effective, therefore it is a kind of excellent renewable material. In addition, due to its antioxidant activity, TA can facilitate the reduction process of GO, and serve as cross-linker to capture graphene sheets during the reduction process [35–37]. Therefore, TA is considered as the environmentally friend reducing agent and stabilizer in graphene synthesis [38]. Researchers have reported the application of TA functionalized rGO in biological monitoring [39, 40]. TA was also used to enhance the mechanical property of rGO electrodes for flexible supercapacitors, but the obtained devices have relatively low area capacitance (238.74 mF cm^{-2}) and energy density (3.6 uWh cm^{-2}) [41–43].

In this study, TA was used as intercalator, cross-linker and reducing agent during the reduction process from GO to rGO at relatively low temperature of 180℃, resulting in fabricating TA/rGO (TrGO) film electrodes for high areal performance supercapacitors. The varying content percentage of TA to GO resulted in the change of electrochemical performance of TrGO. When tested in two-electrode symmetrical supercapacitor with 6 M KOH as electrolyte, TrGO-0.5 exhibited an areal capacitance of 525 mF cm^{-2}, with capacitance retention of 91.7% after 10,000 charging/dicharging cycles. TrGO-0.5 was also assembled into button cell in 2 M $EMIMBF_4$ electrolyte, which shows practical application to light up three LEDs. This research introduces a novel approach to modify rGO film for electrochemical energy storage, resulting in improving the potential of graphene-based electrodes for practical applications.

Experimental sections

Materials

All materials were used directly after purchase. Graphite powder (325 mesh), tannic acid, hydrogen peroxide (H_2O_2, 30%), potassium permanganate ($KMnO_4$, 99.5%), sulfuric acid (H_2SO_4, 95–98%), hydrochloric acid (HCl, 37–38 wt%), potassium hydroxide (KOH), dimethylpyrrolidone (DMF) were bought from Shanghai Sinopsin Chemical Reagent Co., LTD. Polytetrafluoroethylene filter membrane (aperture: ~0.45 μm) and N, N-Dimethylformamide ($EMIMBF_4$) were bought from Jinlong Trading Co., LTD. and Shanghai Yinye Investment Co., LTD., respectively.

Preparation of TrGO electrodes

GO was synthesized via the improved Hummers method, the detailed process was described in supporting materials. To prepare TA/GO films, taking 50 mg of GO, pouring it into 20 ml of DMF. After ultrasonicating for 1 h to obtain GO dispersion, mixing GO with TA at different GO: TA mass ratios (1:0.25; 1:0.5, 1:1, and 1:2) for 30 min under stirring. After ultrasonic dispersion for another 30 min, pouring the mixture into a filter bottle to vacuum filtrate, then air-dry naturally to obtain TA/GO films. The TA/GO films were annealed in a horizontal tube furnace at 180℃ for 2 h (0.5 MPa, N_2 environment) to obtain TrGO films, named as rGO, TrGO-0.25, TrGO-0.5, TrGO-1 and TrGO-2. The fabrication process of TrGO films was illustrated in Fig. 1.

Materials characterization

Scanning electron microscope (SEM, Gemini 500 nCarl Zeiss, Germany) was used to observe the surface and cross-section morphologies of the samples. Raman spectrometer (LAbRAM HR Evolution) was employed for microspectroscopy in the range of 500 ~ 2000 cm^{-1}, with an excitation wavelength of 785 nm. X-ray diffraction (XRD) spectra were obtained in the 5–70° diffraction angle range using PANalytical X-PERT PRO MPD. X-ray photoelectron spectroscopy was analyzed for the surface properties of the electrodes by using an X-ray photoelectron spectrometer (XPS, ESCALAB250Xi).

Electrochemical characterization

The two-electrode cells with 6 M KOH as electrolyte were built to test the electrochemical performance of the samples (Fig. 1). The masses of different electrodes are listed in Table S1. Cyclic voltammetry (CV), Galvanostatic charge-discharge (GCD) and Electrochemical impedance spectroscopy (EIS) measurements of the samples were tested by the electrochemical workstation (CHI660E, Chenhua Instrument, China). The scan rates of CV range from 10 to 500 mV s^{-1} within the voltage window from 0 to 1 V. GCD tests were conducted at current densities from 0.5 to 8 mA cm^{-2} within the potential window from 0 to 1 V. EIS was performed over frequency range from 1 to 1 MHz with 5 mV amplitude. Button cells were also assembled in 2 M $EMIMBF_4$ electrolyte to test the electrochemical performance of TrGO-0.5 via CV (scan rates from 10 to 500 mV s^{-1} with voltages from 0 to 3 V), GCD (current densities from 0.5 to 8 mA cm^{-2} with voltages from 0 to 3 V) and EIS measurements. The cycling stability of TrGO-0.5 was determined by continuous charge-discharge performance at 0.5 mA cm^{-2} for 10,000 cycles. The specific capacitance (C), energy density (E), and power density (P) were calculated based on GCD discharge curves via the equations provided in supporting materials.

Results and discussion

Material characterizations

The surface and cross-section morphologies of the samples were observed via SEM (Fig. 2 and Fig. S1 and S2). Figure 2a illustrates the surface morphology of rGO film, which reveals a typical rippled and folded structure. In Fig. 2b, the planar morphology of TrGO-0.5 film shows the main characteristics of rGO, with additional particles of TA on rGO surface. These TA particles would contribute to the repair of rGO sheets, and create more folds between rGO sheets. Figure 2c and d display the surface morphology of TrGO-2, which shows the accumulation of TA particles on rGO surface due to the excess of TA. This abundance of TA particles may potentially lead to the reduction of TrGO-2 electrochemical performance, as further experiments would confirm. Figure 2e presents the cross-sectional view of rGO electrode, revealing relatively dense arrangement of the rGO layers. However, the SEM of TrGO-0.5 electrode cross-section shows a slight expansion between rGO layers, indicating that TA can alleviate the stacking of rGO layers (Fig. 2f).

Figure 3a displays the XRD patterns of rGO and TrGO samples. The XRD pattern of rGO shows two broad diffraction peaks which correspond to the (002) and (001) crystal planes of graphene, respectively [44, 45]. However, the diffraction peaks of (002) become sharp for the TrGO samples, which indicates that TA can facilitate the reduction process of GO at relatively low temperature of 180 ℃. The Raman spectra of rGO and TrGO samples are shown in Fig. 3b. All samples exhibit two peaks at around ~ 1358 cm^{-1} and ~ 1597 cm^{-1}, corresponding to the D-band and G-band of graphene, respectively. The D-band represents a mixed vibration mode of sp^3 defects, while the G-band indicates in-plane vibrations of sp^2 carbon atoms. The ID/IG ratio is always used to characterize the state of disorder or defects in carbon materials [44–46]. Figure 3c shows that the values of ID/IG of the samples first increase from 1.23 (rGO) to 1.41 (TrGO-1), and then decrease to 1.15 (TrGO-2), indicating that the introduction of TA to rGO not only plays a certain reducing effect but also generates some defects. However, it is not the case that excessive introduction of TA can achieve the best results.

The surface elemental composition and chemical bonding states of the samples were examined by XPS. As shown in Fig. 3d, the XPS spectra of rGO and TrGO-0.5 indicate that they are mainly composed of C1s and O1s (The carbon and oxygen contents are listed in Table S2). The three peaks at about 284.5, 286, and 288.4 eV can be assigned to C-C/C = C, C-O, and O = C-O chemical bonds, respectively (Fig. 3e and f). It is noteworthy that the intensity of C-O peak of TrGO-0.5 is higher than that of rGO, caused by the rich oxygen-containing groups of TA (such as phenolic hydroxyl and carboxyl groups) in TrGO-0.5. The oxygen content of TrGO-0.5 is 17.23 at%, and it is 15.08 at% for rGO (Table S2). The higher oxygen content of TrGO-0.5 also indicates that the main functional groups of TA still exist after mild thermal reduction process of TA/GO film at 180 ℃.

Electrochemical performance

The electrochemical performances of the samples were tested via two-electrode symmetric cell in 6 M KOH

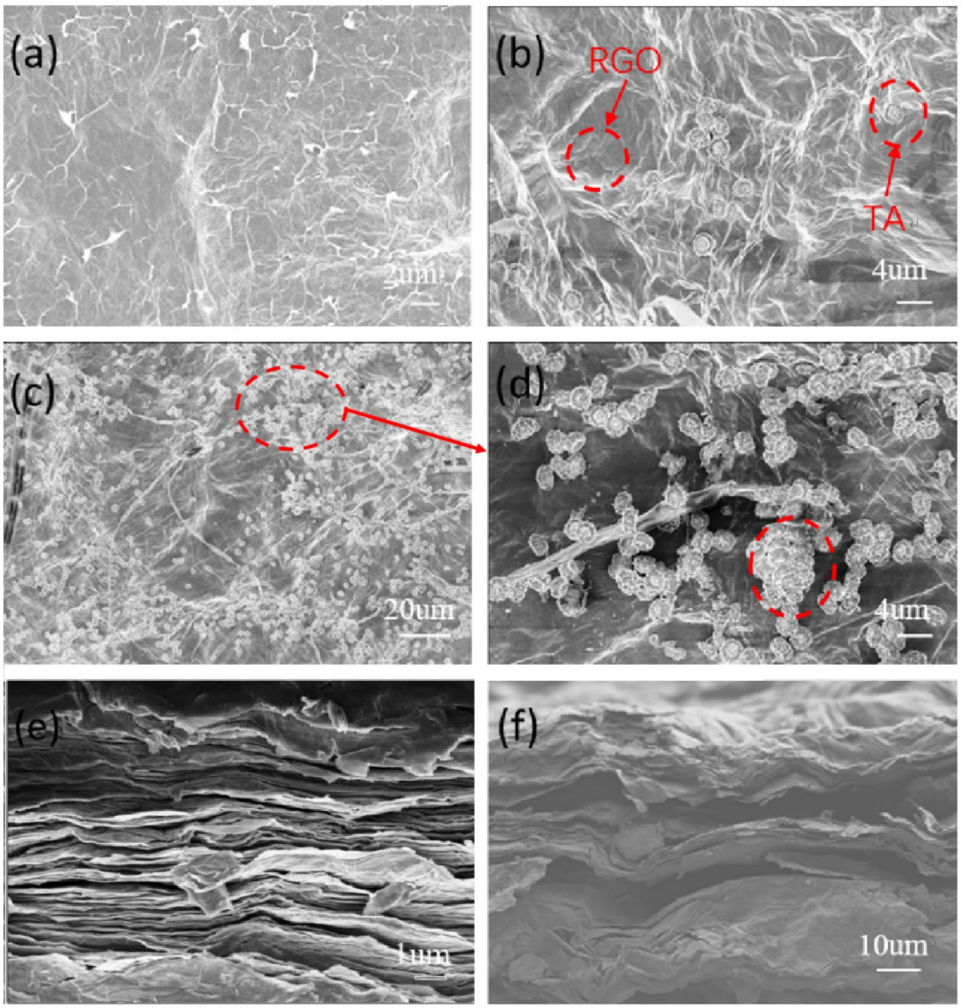

Fig. 2 The surface and cross-section morphologies of samples. **a**, **b** The SEM images of rGO and TrGO-0.5. **c**, **d** The SEM images of TrGO-2 at different magnification scale. **e**, **f** The cross-sectional SEM images of rGO and TrGO-0.5

electrolyte. Figure 4a shows the CV curves of the rGO and TrGO electrodes at scan rate of 200 mV s^{-1}. Obviously, the introduction of TA does increase the specific capacitance of rGO, and TrGO-0.5 has the largest integrated area of the CV curve. The GCD results at current density of 0.5 mA cm^{-2} also show that TrGO-0.5 has the highest specific capacitance among the samples (Fig. 4b). TrGO-1 and TrGO-2 have lower specific capacitance than that of TrGO-0.5, possibly because the higher content of TA in TrGO-1 and TrGO-2 would lead to partial blockage of some micropores in rGO, resulting in lower transfer ability of electrolyte ions in TrGO-1 and TrGO-2. However, if the content of TA is too low, the effect of TA would not fully play. Therefore, TrGO-0.25 also has lower specific capacitance than that of TrGO-0.5, which can be observed from the CV and GCD curves (Fig. S1). The CV and GCD curves of TrGO electrodes illustrate their main EDL capacitance accompanied by partial pseudocapacitance.

The CV curves of TrGO-0.5 at scan rates from 10 to 500 mV s^{-1} are shown in Fig. 4c, and its GCD curves at current densities from 0.5 to 8 mA cm^{-2} are displayed in Fig. 4d. Based on the GCD discharge curves, the areal capacitance and mass capacitance of rGO and TrGO-0.5 (Fig. 4e and f) are calculated according to the formula in supporting material (S1, S2). The areal capacitances of rGO and TrGO-0.5 are 434 and 525 mF cm^{-2} at 0.5 mA cm^{-2} (Fig. 4e), and their mass capacitances are 134 and 147 F g^{-1} at 0.2 A g^{-1} (Fig. 4f), respectively. Table 1 presents the performance comparison of TrGO-0.5 with some reported rGO-based materials [47–53], such as the rGO/$Ti_3C_2T_x$ composite (115 F g^{-1} at 0.2 A g^{-1}) [48] and the rGO/ZnO composite (60 F g^{-1} at 5 mv s^{-1}) [53]. Appropriate TA content can not only promote the reduction of GO but also alleviate the stacking of rGO sheets and provide some redox active sites, resulting in the specific capacitance increase of TrGO-0.5.

The analysis of EIS data would reveal the information regarding ion diffusion resistance and transport ability. Figure 4g shows the Nyquist plots of rGO and TrGO-0.5 (The equivalent circuit diagram of TrGO-0.5 electrode is shown in Fig. S2). In the low frequency region, the higher curve slope of TrGO-0.5 compared to that of rGO indicates that TrGO-0.5 has better capacitive response than rGO. Therefore, the

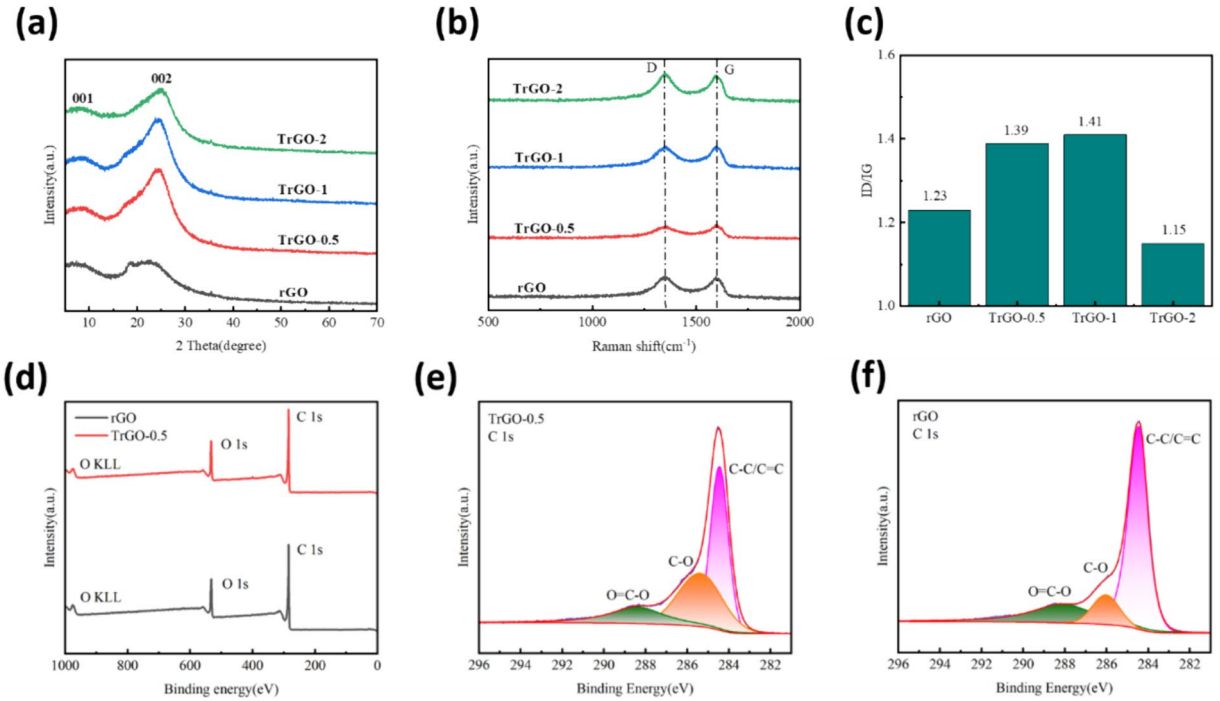

Fig. 3 **a** XRD spectra of rGO and TrGO samples. **b**, **c** Raman spectra and ID/IG of rGO and TrGO samples. **d** XPS spectra of rGO and TrGO-0.5. **e**, **f** High resolution of the C1s spectra of TrGO-0.5 and rGO

introduction of TA indeed enhances the ions diffusion and transfer kinetics in TrGO-0.5. At high-frequency region (the insert in Fig. 4g), the intersection of Nyquist plot with the x-axis corresponds to the equivalent series resistance (ESR), which includes the intrinsic resistance of the electrode and collector, the diffusion resistance of the electrolyte, and the contact resistance at electrode-electrolyte interface [54]. Both rGO and TrGO-0.5 exhibit low ESR which is about 2 Ω. The Bode phase plots (Fig. 4h) show that the phase angle of rGO at low frequencies is 65.9°, while that of TrGO-0.5 increases to 78.3°. Therefore, the phase angle of TrGO-0.5 is closer to 90° compared to that of rGO, which also indicates that TrGO-0.5 has more ideal capacitive behavior. According to the formula of $C'' = Z'/2\pi f|Z|^2$ [55], in which C", Z' and Z are the virtual capacitance, the imaginary part and the modulus value of the impedance, respectively, the virtual capacitances of rGO and TrGO-0.5 are calculated and plotted versus frequency (Fig. 4i). The time electrostatic constant τ ($\tau = 1/f_o$) of rGO and TrGO-0.5 are 70.43 and 5.61s, respectively, where f_o is the frequency corresponding to the maximum virtual capacitance. The much shorter τ of TrGO-0.5 indicates that it has faster frequency response and ion transfer rate, which is consistent with the results shown in the Nyquist and Bode plots.

To further investigate the charge storage mechanism of the electrodes, the relationship between peak current (i) and scan rate (v) is calculated according to the

Table 1 Performance comparison of this work with some reported results

Electrode material	Electroyle	Capacitance	Electochemical testing	ref
RGO/TA	1 M H_2SO_4	238.74mF cm^{-2} at 1 mA cm^{-2}	Three electrodes in Ag/AgCl	[42]
RGO/$SiVW_{11}$	0.5 M H_2SO_4	377.4mF cm^{-2} at 1.5 mA cm^{-2}	Button cell	[49]
RGO/Ti_3C_2Tx	6 M KOH	115F $^{g-1}$ at 0.2 A $^{g-1}$	Symmetrical two-electrode	[50]
RGO/PPy	1 M H_2SO_4	631mF cm^{-2} at 1mA cm^{-2}	An Ag/AgCl as reference electrode	[51]
RGO/CNT/ANF	6 M KOH	79F $^{g-1}$ at 200mv $^{s-1}$	Button cell	[52]
RGO/AC/CNT	1 M $LiClO_4$	101F $^{g-1}$ at 0.2A $^{g-1}$	Button cell	[53]
RGO/$MnCO_3$	1 M Na_2SO_4	468mF cm^{-2} at 2.8mA cm^{-2}	Three-electrode cells	[54]
RGO/ZnO	1 M KCl	60.63F $^{g-1}$ at 5mv $^{s-1}$	Three-electrode cells	[55]
This work	6 M KOH	520mF cm^{-2} at 0.5mA cm^{-2}/147F $^{g-1}$ at 0.2A $^{g-1}$	Symmetrical two-electrode	

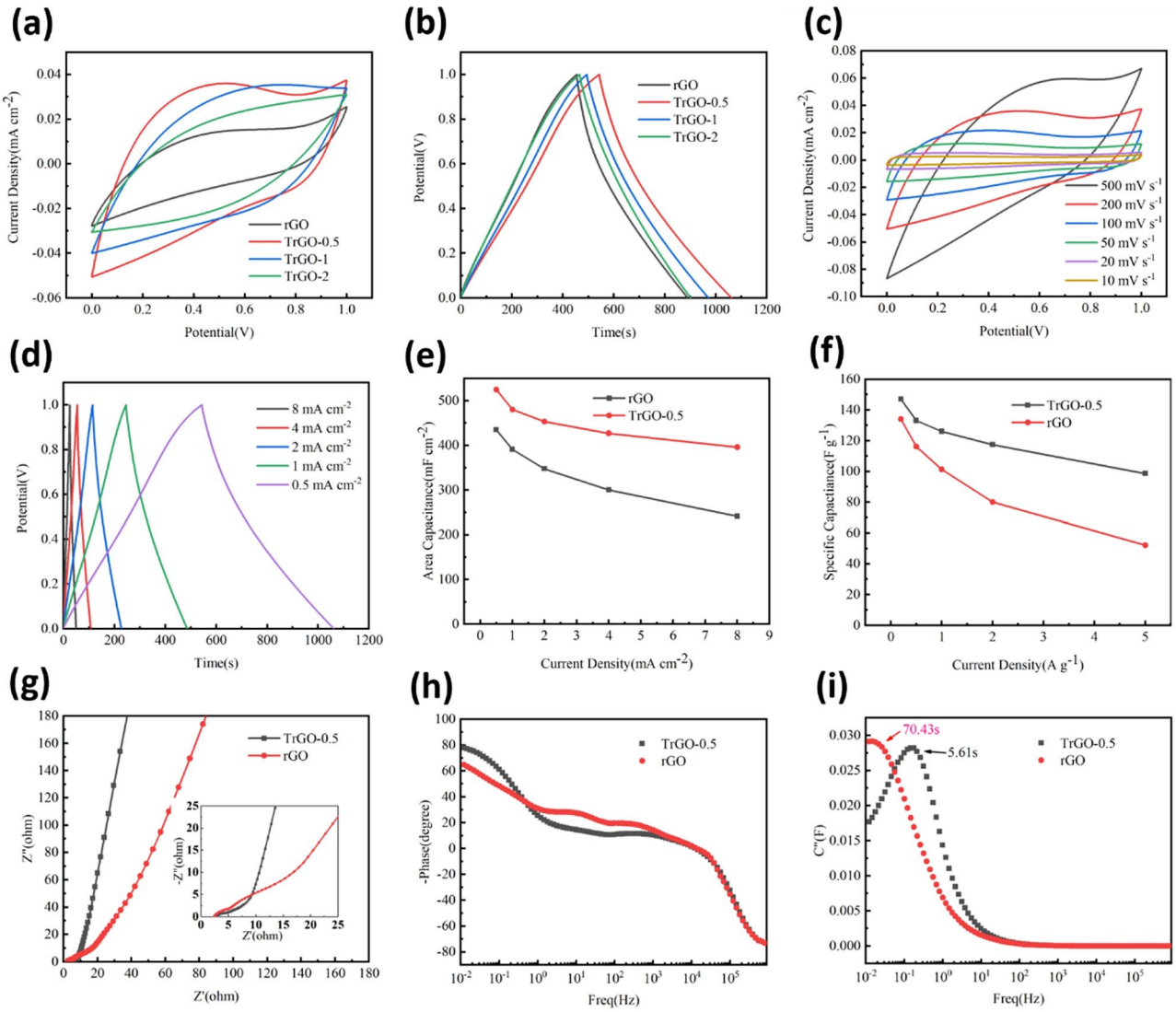

Fig. 4 **a** CV curves of rGO and TrGO electrodes at scan rate of 200 mV s^{-1}. **b** GCD curves of rGO and TrGO electrodes at current density of 0.5 mA cm^{-2}. **c** CV curves of TrGO-0.5 at different scan rates. **d** GCD curves of TrGO-0.5 at different current densities. **e** Area capacitance of rGO and TrGO-0.5 at different current densities. **f** Mass capacitance of rGO and TrGO at different current densities. **g** Nyquist plots of rGO and TrGO-0.5, the insert is the enlarged high-frequency region. **h** Bode plots of phase angle versus frequency of rGO and TrGO. **i** Relationship between imaginary capacitance and frequency of rGO and TrGO-0.5. The electrochemical performances were all tested in two-electrode symmetrical cells in 6 M KOH electrolyte

formulai = av^b, where parameters a and b are adjustable. The b value of 0.5 indicates surface-controlled behavior, while the b value of 1 represents diffusion-controlled process. The b values for rGO, TrGO-0.5, TrGO-1 and TrGO-2 are calculated to be 0.81, 0.92, 0.88 and 0.86, respectively, as shown in Fig. 5a. The results suggest that all electrodes exhibit a combination of diffusion-controlled and surface-controlled capacitance behavior, and the introduction of TA leading to more influence of diffusion process. Furthermore, the contributions of surface capacitance and diffusion capacitance can be calculated by equation (S9) (Fig. 5b). The specific capacitance of rGO is primarily composed of surface capacitance, with small portion of diffusion capacitance. However, with the introduction of TA, the diffusion capacitance increases. This indicates that TA can additionally enhance pseudocapacitive contribution, when reaching its maximum in TrGO-0.5 electrode. However, excessive introduction of TA may lead to the decrease of the active sites, and cause the surface micropores of rGO to be

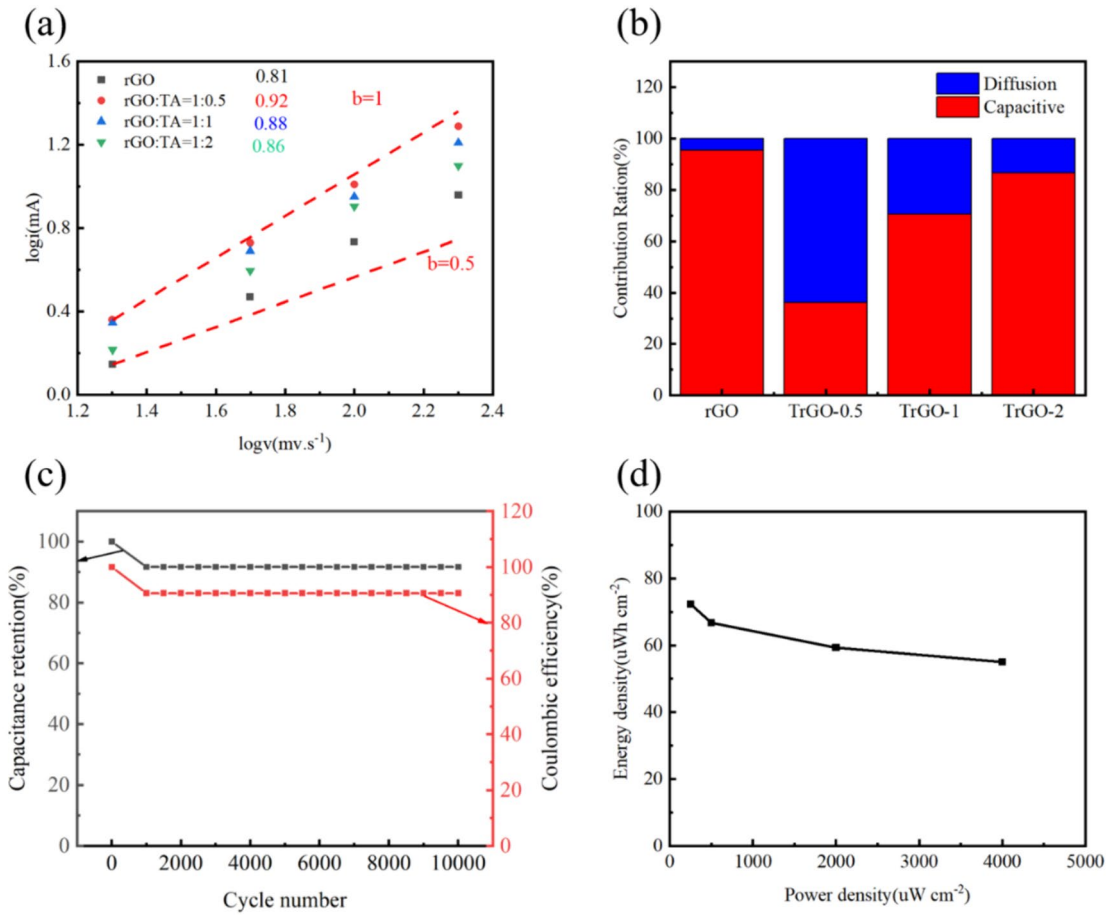

Fig. 5 **a** Logarithmic plot of peak current as a function of scan rate. **b** Capacitance contribution of the rGO and TrGO electrodes at the scan speed of 20 mV s^{-1}, the red area represents the surface capacitance, and the blue area represents the diffusion capacitance. **c** Cycling performance and Coulombic efficiency of TrGO-0.5 tested at 5 A g^{-1}. **d** The plot of energy density with power density (Ragone plot) of TrGO-0.5

blocked, resulting in the decrease of diffusion capacitance. Therefore, from TrGO-0.5 to TrGO-1 and TrGO-2, their diffusion capacitance keeps decreasing. TrGO-0.5 also shows excellent cycling stability and Coulombic efficiency. After 10,000 cycles at current density of 4 mA cm^{-2}, its capacitance retention and Coulombic efficiency are 91.7% and 90.6%, respectively (Fig. 5c). The energy density of TrGO-0.5 can reach 72.2 uWh cm^{-2} at power density of 250.9 uW cm^{-2}. When the power density was increased to 4000.6 uW cm^{-2}, TrGO-0.5 still has high energy density of 55.03 uWh cm^{-2} (Fig. 5d).

For the practical application, TrGO-0.5 was also assembled to button cell in 2 M $EMIMBF_4$ electrolyte, its potential window can reach 3 V [14] (Fig. 6). Both CV (Fig. 6a) and GCD (Fig. 6b) curves indicate the good capacitive behavior of TrGO-0.5 in $EMIMBF_4$ electrolyte. Nyquist plot shows the about 45° slope at low-frequency region (Fig. 6c) and ESR of 4.5 Ω (insert in Fig. 6c). The diameter of the semicircle in high-frequency region is related to the ion transfer resistance at electrode and electrolyte interface. It is about 384.2 Ω for TrGO-0.5 in $EMIMBF_4$ (Fig. 6c), significantly higher than that in 6 M KOH (the insert in Fig. 4g). Additionally, we also tested the cyclic stability and Coulombic efficiency of TrGO-0.5 based button cell (Fig. 6d). After 10,000 charge/discharge cycles at 2 mA cm^{-2}, the capacitance retention and Coulombic efficiency are 53% and 90.1%, respectively. Ragone plot shows that TrGO-0.5 has decent energy density of 10 Wh kg^{-1} at power density of 300.2 W kg^{-1}, which is superior than some recent reported carbon based materials [47, 56–58] (Fig. 6e). This TrGO-0.5 based button cell can light up three LEDs on a breadboard (Fig. 6f), which indicates its potential for practical application.

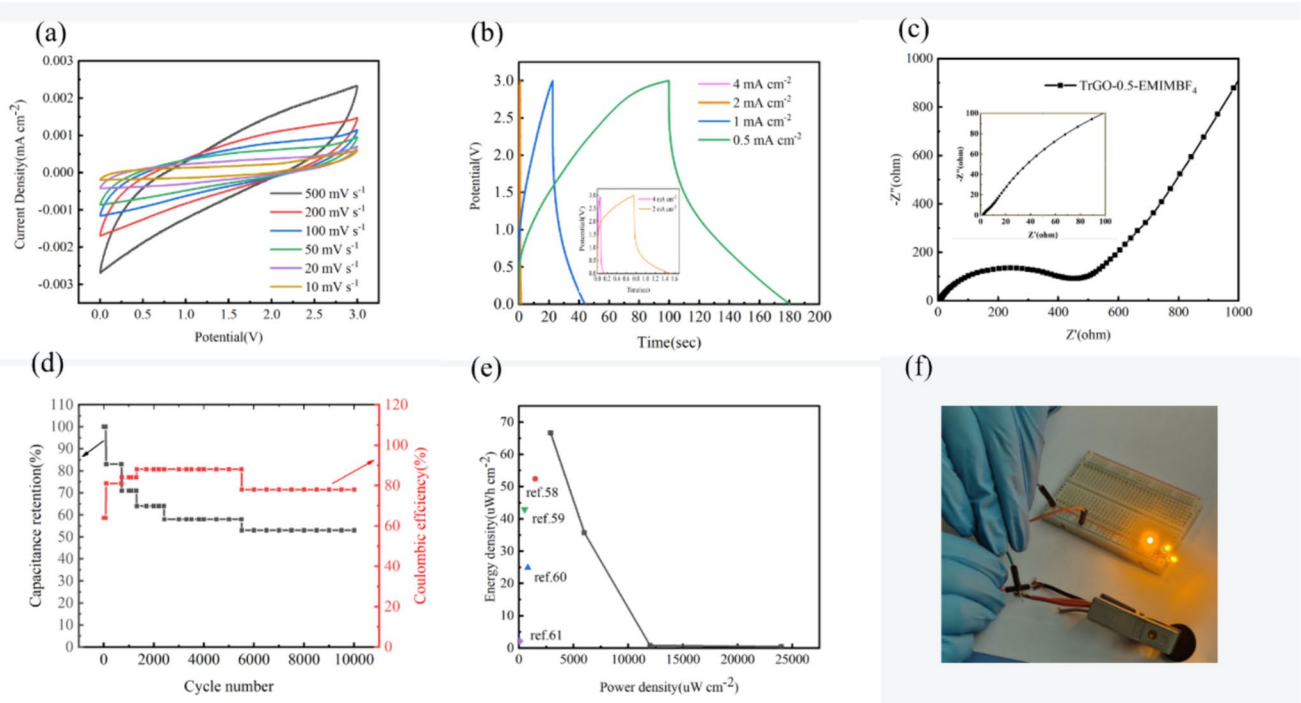

Fig. 6 Electrochemical performance of TrGO-0.5 based button cell in 2 M $EMIMBF_4$ electrolyte. **a** CV curves at different scan rates. **b** GCD curves at different current densities. **c** Nyquist plot. **d** Cycle stability and Coulombic efficiency tested at 4 mV cm^{-2}. **e** Ragone plot. **f** Illustration of TrGO-0.5 based button cell to light up three LEDs

Conclusion

In summary, we synthesized TrGO layered films by modifying the rGO sheets with TA molecules for supercapacitor, resulting in enhanced areal electrochemical performance. Specifically, when tested in two-electrode symmetrical cell with 6 M KOH electrolyte, the TrGO-0.5 gives area capacitance of 525 mF cm^{-2} at 0.5 mA cm^{-2}, energy density of 72.2 uWh cm^{-2} at power density of 250.9 uW cm^{-2}. It also has excellent cycling stability of 91.7% retention after 10,000 charging/discharging cycles at current density of 4 mA cm^{-2}. TrGO-0.5 was also assembled to button cell in 2 M $EMIMBF_4$ electrolyte for practical application, and it can light up three LEDs. Our study provides experimental evidence for the preparation of TrGO electrodes by introducing TA to modify the rGO sheets for practical application.

Supplementary Information The online version contains supplementary material available at https://doi.org/10.1007/s10008-024-05946-y.

Acknowledgements This work was supported by the National Natural Science Foundation of China (No.52273239, 52271208) and Innovation and Entrepreneurship Training Program for College Students (S202310359261).

References

1. Sharma K, Arora A, Tripathi SK (2019) Review of supercapacitors: materials and devices. J Energy Storage 21:801–825
2. Yaseen M, Khattak MAK, Humayun M, Usman M, Shah SS, Bibi S, Ullah H (2021) A review of supercapacitors: materials design, modification, and applications. Energies 14(22):7779
3. Lemian D, Bode F (2022) Battery-supercapacitor energy storage systems for electrical vehicles: a review. Energies 15(15):5683
4. Liu L, Feng Y, Wu W (2019) Recent progress in printed flexible solid-state supercapacitors for portable and wearable energy storage. J Power Sources 410:69–77
5. Yang H, Kannappan S, Pandian AS, Jang JH, Lee YS, Lu W (2017) Graphene supercapacitor with both high power and energy density. Nanotechnology 28(44):445401
6. Dong W, Xie M, Zhao S, Qin Q, Huang F (2023) Materials design and preparation for high energy density and high power density electrochemical supercapacitors. Mater Sci Eng R: Rep 152:100713
7. Reina M, Scalia A, Auxilia G, Fontana M, Bella F, Ferrero S, Lamberti A (2022) Boosting Electric double layer Capacitance in Laser Induced Graphene based supercapacitors. Adv Sustainable Syst 6(1):2100228
8. Park HW, Roh KC (2023) Recent advances in and perspectives on pseudocapacitive materials for supercapacitors-a review. J Power Sources 557:232558
9. Rychagov AY, Sosenkin VE, Izmailova MY, Kabachkov EN, Shulga YM, Volfkovich YM, Gutsev GL (2023) Self-discharge processes in symmetrical supercapacitors with activated Carbon electrodes. Materials 16(19):6415

10. Inal IIG, Aktas Z (2020) Enhancing the performance of activated carbon based scalable supercapacitors by heat treatment. Appl Surf Sci 514:145895
11. Liu L, Niu Z, Chen J (2018) Flexible supercapacitors based on carbon nanotubes. Chin Chem Lett 29(4):571–581
12. Komatsubara K, Suzuki H, Inoue H, Kishibuchi M, Takahashi S, Marui T, Hayashi Y (2022) Highly oriented carbon nanotube supercapacitors. ACS Appl Nano Mater 5(1):1521–1532
13. Zhai S, Chen Y (2022) Graphene-based fiber supercapacitors. Acc Mater Res 3(9):922–934
14. Li J, Tang J, Yuan J, Zhang K, Shao Q, Sun Y, Qin LC (2016) Interactions between graphene and ionic liquid electrolyte in supercapacitors. Electrochim Acta 197:84–91
15. Eftekhari A, Li L, Yang Y (2017) Polyaniline supercapacitors. J Power Sources 347:86–107
16. Banerjee J, Dutta K, Kader MA, Nayak SK (2019) An overview on the recent developments in polyaniline-based supercapacitors. Polym Adv Technol 30(8):1902–1921
17. Yavuz A, Ozdemir N, Zengin H (2020) Polypyrrole-coated tape electrode for flexible supercapacitor applications. Int J Hydrog Energy 45(38):18876–18887
18. Tian Y, Yang C, Song X, Liu J, Zhao L, Zhang P, Gao L (2019) Engineering the volumetric effect of Polypyrrole for auto-deformable supercapacitor. Chem Eng J 374:59–67
19. Vadiyar MM, Liu X, Ye Z (2019) Macromolecular polyethynylbenzonitrile precursor-based porous covalent triazine frameworks for superior high-rate high-energy supercapacitors. ACS Appl Mater Interfaces 11(49):45805–45817
20. Luo T, Xu X, Jiang M, Lu YZ, Meng H, Li CX (2019) Polyacetylene carbon materials: facile preparation using $AlCl_3$ catalyst and excellent electrochemical performance for supercapacitors. RSC Adv 9(21):11986–11995
21. Chen H, Zeng S, Chen M, Zhang Y, Li Q (2017) A new insight into the rechargeable mechanism of manganese dioxide based symmetric supercapacitors. RSC Adv 7(14):8561–8566
22. Han ZJ, Pineda S, Murdock AT, Seo DH, Ostrikov KK, Bendavid A (2017) RuO_2-coated vertical graphene hybrid electrodes for high-performance solid-state supercapacitors. J Mater Chem A 5(33):17293–17301
23. Phakkhawan A, Suksangrat P, Srepusharawoot P, Ruangchai S, Klangtakai P, Pimanpang S, Amornkitbamrung V (2022) Reagent- and solvent-mediated Fe_2O_3 morphologies and electrochemical mechanism of Fe_2O_3 supercapacitors. J Alloys Compd 919:165702
24. Wang G, Zhang L, Zhang J (2012) Rev Electrode Mater Electrochem Supercapacitors 41(2):797–828
25. Su H, Zhang H, Liu F, Chun F, Zhang B, Chu X, Yang W (2017) High power supercapacitors based on hierarchically porous sheet-like nanocarbons with ionic liquid electrolytes. Chem Eng J 322:73–81
26. Chang H, Wu H (2013) Graphene-based nanocomposites: preparation, functionalization, and energy and environmental applications. Energy Environ Sci 6(12):3483–3507
27. Stoller MD, Park S, Zhu Y, An J, Ruoff RS (2008) Graphene-based ultracapacitors. Nano Lett 8(10):3498–3502
28. Liu Y, Zeng Z, Sharma RK, Gbewonyo S, Allado K, Zhang L, Wei J (2019) A bi-functional configuration for a metal-oxide film supercapacitor. J Power Sources 409:1–5
29. Nandi D, Mohan VB, Bhowmick AK, Bhattacharyya D (2020) Metal/metal oxide decorated graphene synthesis and application as supercapacitor: a review. J Mater Sci 55:6375–6400
30. Wang Y, Ding Y, Guo X, Yu G (2019) Conductive polymers for stretchable supercapacitors. Nano Res 12:1978–1987
31. Lin Y, Dai H, Su S, Zhu X (2024) A pretreated-carbon cloth/polypyrrole/rGO electrode material with enhanced hydrophilicity and low impedance for flexible quasi-solid supercapacitors. J Solid State Electrochem 28(2):495–506
32. Borenstein A, Hanna O, Attias R, Luski S, Brousse T, Aurbach D (2017) Carbon-based composite materials for supercapacitor electrodes: a review. J Mater Chem A 5(25):12653–12672
33. Yang Q, Wang W, Li X, Li Q, Xun M, Meng L, Xu J (2023) Nitrogen doping in the surface layers of Ti3C2Tx/rGO film via nitrogen ion implantation for supercapacitor. J Solid State Electrochem 27:1955–1967
34. Li Z, Xu K, Pan Y (2019) Recent development of supercapacitor electrode based on carbon materials. Nanatechnol Reviews 8(1):35–49
35. Kwon YB, Go SH, Choi C, Seo TH, Yang B, Lee MW, Kim YK (2021) Simultaneous reduction and functionalization of graphene oxide sheets with tannic acid for a strong composite material with multi-modally interactive interfaces. Diam Relat Mater 119:108565
36. Kwon YB, Lee SR, Seo TH, Kim YK (2022) Fabrication of a strong artificial nacre based on tannic acid-functionalized graphene oxide and poly (vinyl alcohol) through their multidentate hydrogen bonding. Macromol Res 30(4):279–284
37. Zubir MNM, Badarudin A, Kazi SN, Huang NM, Misran M, Sadeghinezhad E, Yusoff N (2015) Highly dispersed reduced graphene oxide and its hybrid complexes as effective additives for improving thermophysical property of heat transfer fluid. Int J Heat Mass Transf 87:284–294
38. Lei Y, Tang Z, Liao R, Guo B (2011) Hydrolysable tannin as environmentally friendly reducer and stabilizer for graphene oxide. Green Chem 13(7):1655–1658
39. Chen H, Wang M, Wang L, Zhou M, Wu H, Yang H (2021) Enhanced separation performance of Hg^{2+} in desulfurization wastewater using a tannin acid reduced graphene oxide membrane. Sep Purif Technol 274:119017
40. Tang CY, Yu P, Tang LS, Wang QY, Bao RY, Liu ZY, Yang W (2018) Tannic acid functionalized graphene hydrogel for organic dye adsorption. Ecotoxicol Environ Saf 165:299–306
41. Flouda P, Yun J, Loufakis D, Shah SA, Green MJ, Lagoudas DC, Lutkenhaus JL (2020) Structural reduced graphene oxide supercapacitors mechanically enhanced with tannic acid. 4:2301–2308
42. Yang C, Yang J, Liang C, Zang L, Zhao Z, Li H, Bai L (2021) Flexible supercapacitors with tunable capacitance based on reduced graphene oxide/tannin composite for wearable electronics. J Electroanal Chem 894:115354
43. Xu L, Yu H, Li Y, Jia M, Yao C, Jin XJ (2018) Tannic acid-decorated spongy graphene for flexible and high performance supercapacitors. J Electrochem Soc 165(9):A1706–A1712
44. Park S, An J, Jung I, Piner RD, An SJ, Li X, Ruoff RS (2009) Colloidal suspensions of highly reduced graphene oxide in a wide variety of organic solvents. Nano Lett 9(4):1593–1597
45. Yang W, Gao Z, Wang J, Wang B, Liu Q, Li Z, Liu L (2012) Synthesis of reduced graphene nanosheet/urchin-like manganese dioxide composite and high performance as supercapacitor electrode. Electrochim Acta 69:112–119
46. Cançado LG, Takai K, Enoki T, Endo M, Kim YA, Mizusaki H, Pimenta MA (2006) General equation for the determination of the crystallite size L_a of nanographite by Raman spectroscopy. Appl Phys Lett 88(16):163106
47. Biradar BR, Maity S, Chandewar PR, Shee D, Das PP, Mal SS (2023) High areal capacitance polyoxotungstate-reduced graphene oxide-based supercapacitors. Inorg Chem Commun 155:110987
48. Yang Q, Wang W, Li X, Li Q, Xun M, Meng L, Xu J (2023) Nitrogen doping in the surface layers of $Ti_3C_2T_x$/rGO film via nitrogen ion implantation for supercapacitor. J Solid State Electrochem 27:1955–1967
49. Zhu F, She X, Zhang Z, Yu X, Ji J, Li L, Li S (2024) Flexible reduced graphene oxide/polypyrrole films for supercapacitors. Diam Relat Mater 141:110581
50. Patel A, Loufakis D, Flouda P, George I, Shelton C, Harris J, Lutkenhaus JL (2020) Carbon nanotube/reduced graphene oxide/

aramid nanofiber structural supercapacitors. ACS Appl Energy Mater 3(12):11763–11771
51. Li X, Tang Y, Song J, Yang W, Wang M, Zhu C, Lin Y (2018) Self-supporting activated carbon/carbon nanotube/reduced graphene oxide flexible electrode for high performance supercapacitor. Carbon 129:236–244
52. Jana M, Samanta P, Murmu NC, Kuila T (2017) Morphology controlled synthesis of $MnCO_3$-RGO materials and their supercapacitor applications. J Mater Chem A 5(25):12863–12872
53. Ghorbani M, Golobostanfard MR, Abdizadeh H (2017) Flexible freestanding sandwich type ZnO/rGO/ZnO electrode for wearable supercapacitor. Appl Surf Sci 419:277–285
54. Zhang X, Xiao P, Feng X (2017) Toward combining thematic information with hierarchical multiscale segmentations using tree Markov random field model. ISPRS J Photogrammetry Remote Sens 131:134–146
55. Zhao C, Wang Q, Zhang H, Passerini S, Qian X (2016) Two-dimensional titanium carbide/RGO composite for high-performance supercapacitors. ACS Appl Mater Interfaces 8(24):15661–15667
56. Xu C, Wang X, Liu K, Yu J, Zhang J, Jiang M (2023) Fabrication of flexible micro-supercapacitors based on low-oxidized graphene/polyaniline/porous carbon ternary composites with high area capacitance. J Science: Adv Mater Devices 8(4):100643
57. Young C, Chen HT, Guo SZ (2022) Highly porous holey carbon for high areal energy density solid-state supercapacitor application. Micromachines 13(6):916
58. Yue Y, Liu N, Ma Y, Wang S, Liu W, Luo C, Gao Y (2018) Highly self-healable 3D microsupercapacitor with MXene–graphene composite aerogel. ACS Nano 12(5):4224–4232